JACS
JOURNAL OF THE AMERICAN CHEMICAL SOCIETY
pubs.acs.org/JACS
Article

New Compounds and Phase Selection of Nickel Sulfides via Oxidation State Control in Molten Hydroxides

Xiuquan Zhou, David J. Mandia, Hyowon Park, Mahalingam Balasubramanian, Lei Yu, Jianguo Wen, Andrey Yakovenko, Duck Young Chung, and Mercouri G. Kanatzidis*

Cite This: *J. Am. Chem. Soc.* 2021, 143, 13646−13654
Read Online
ACCESS | Metrics & More | Article Recommendations | Supporting Information

ABSTRACT: Molten salts are promising reaction media candidates for the discovery of novel materials; however, they offer little control over oxidation state compared to aqueous solutions. Here, we demonstrated that when two hydroxides are mixed, their melts become fluxes with tunable solubility, which are surprisingly powerful solvents for ternary chalcogenides and offer effective paths for crystal growth to new compounds. We report that precise control of the oxidation state of Ni is achievable in mixed molten LiOH/KOH to grow single crystals of all known ternary K−Ni−S compounds. It is also possible to access several new phases, including a new polytope of β-$K_2Ni_3S_4$, as well as low-valence KNi_4S_2 and $K_4Ni_9S_{11}$. KNi_4S_2 is a two-dimensional low-valence nickel-rich sulfide, and β-$K_2Ni_3S_4$ has a hexagonal lattice. Moreover, using KNi_4S_2 as a template, we obtained a new layered binary Ni_2S by topotactic deintercalation of K. The new binary Ni_2S has a van der Waals gap and can function as a new host layer for intercalation chemistry, as demonstrated by the intercalation of LiOH between its layers. The oxidation states of low-valence KNi_4S_2 and Ni_2S were studied using X-ray absorption spectroscopy and X-ray photoelectron spectroscopy. Density functional theory calculations showed large antibonding interactions at the Fermi level for both KNi_4S_2 and Ni_2S, corresponding to the flat-bands with large Ni-$d_{x^2-y^2}$ character.

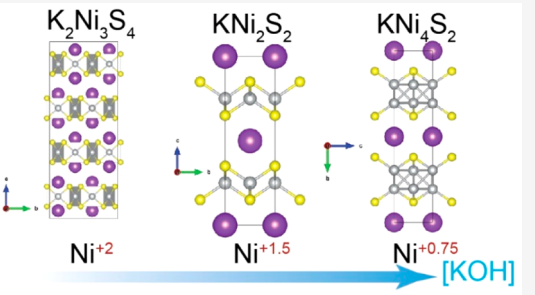

INTRODUCTION

High-temperature fluxes are a great tool for material synthesis because they offer moderate temperature regimes, crystal growth, and kinetic stabilization of compounds that cannot be prepared by direct high-temperature synthesis.[1−6] Reactions conducted in fluxes have been exploited to discover materials, such as complex metal oxides, chalcogenides, and pnictides. These materials exhibit diverse properties, such as large optical nonlinearities, ion-exchange, high critical temperature (T_c) superconductivity, high-performance thermoelectricity, and photovoltaic conversion.[6−11] However, like most solid-state syntheses, the "black-box" nature of high-temperature fluxes offers little or no insight into solvated species, reaction mechanisms, intermediates, or nucleation. Thus, without adequate knowledge of these reaction processes, compound design for extended solids that begins at the molecular level lags behind organic synthesis, in which molecules can be planned step-by-step on a drawing board via retrosynthesis. Contrary to organic synthesis, the science of solid-state inorganic synthesis is still in an early stage.

In an effort to pursue a more targeted and rational approach toward the synthesis of new compounds, panoramic reactions using *in situ* diffraction techniques to monitor the dissolution, intermediates, and products in a flux reaction have provided great insight into reaction mechanisms with different fluxes.[12−16] For example, Shoemaker et al. discovered that varying the [S] in the polysulfide flux of K_xS_y could lead to a change in the CuS_4 motifs in the local coordination.[13] To achieve the goal of rational material synthesis with the knowledge gained from panoramic synthesis, a tunable flux is required to shift the reaction paradigm toward targeted compounds or structures and away from known compounds. Hence, we recently formulated a solution using AOH/AX mixtures (A = alkali metals and X = halides) with tunable solubility. An increase in the concentration [OH] can shift the reaction paths in favor of more complex and kinetically stable products with lower solubility. Moreover, building blocks from different thermodynamic products may be combined to form heterolayers in a kinetically controlled pathway.

Chalcophilic elements like Ni have very low solubilities in mixed LiOH/LiCl ([OH] = 0.5−1) and only trivial binaries like Ni_3S_2 were obtained. However, increasing the solubility can shift the reaction paradigm toward more complex structures. Thus, in this study, we demonstrated the effectiveness of the tunable flux by varying the LiOH/KOH

Received: May 18, 2021
Published: August 19, 2021

https://doi.org/10.1021/jacs.1c05107
J. Am. Chem. Soc. 2021, 143, 13646−13654

ratio in different chalcogenides, including K−Ni−S ternaries. Ternary K−Ni−Q (Q = S and Se) systems have been well studied over the past decade, especially the tetragonal KNi_2Q_2 ($I4/mmm$), because of their close structural proximity to Fe-based superconductors.[17−22] To date, there are two reported ternary systems, α-$K_2Ni_3S_4$ and the low-valence KNi_2S_2 (Figures 1a and b, respectively). KNi_2S_2 is isostructural to

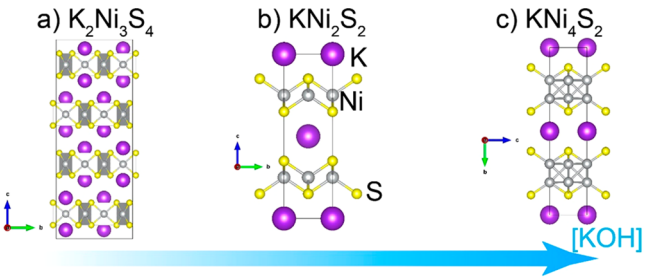

Figure 1. Crystal structures of (a) $K_2Ni_3S_4$, (b) KNi_2S_2, and (c) KNi_4S_2.

the superconducting 122-type KFe_2Se_2 and exhibits exotic physical behavior,[20] including superconductivity below 0.46 K. Although the T_c is quite low, it is interesting, nonetheless, as its superconductivity rises after the suppression of the charge density wave (CDW).[20] It is also suspected to exhibit heavy fermion character in its superconductivity similar to that of KNi_2Se_2 and $TlNi_2S_2$.[19,21]

Herein, we have reported the synthesis of all known ternaries of the K−Ni−S systems, α-$K_2Ni_3S_4$,[23] KNi_2S_2[24] additional new ternaries of β-$K_2Ni_3S_4$, KNi_4S_2 (Figure 1c), and $K_4Ni_9S_{11}$ obtained by varying the LiOH/KOH ratio. Although mixed hydroxides have been used to grow crystals of oxides, they have primarily been used with ratios that led to the lowest eutectic melting point for lowering the reaction temperature. This could be beneficial for avoiding vaporization of starting materials because these reactions are often carried out in open crucibles.[5,6] In contrast, we varied the ratio of LiOH/KOH instead of using a fixed ratio. Moreover, the synthesis of chalcogenides in molten hydroxide medium has never been reported prior to our study. Finally, we discovered a correlation between the oxidation states of Ni (+2, +1.5, and +1−0.75) and basicity ([KOH]). Increasing [KOH] leads to a lower Ni oxidation state in the K−Ni−S ternaries. We can achieve phase selection for the known compounds, $K_2Ni_3S_4$ and KNi_2S_2, and for a new compound, KNi_4S_2, using this unexpected phenomenon. This selection method, which is dependent on the basicity instead of the starting materials, offers a facile route for the synthesis and crystal growth of K−Ni−S ternaries. The reaction pathways observed here could have implications for the synthesis of other systems involving transition metals. This could be of synthetic utility for developing rational strategies for synthesizing broad sets of new compounds.

RESULTS AND DISCUSSION

Synthesis and Crystal Structures. The hydroxide fluxes allow the use of simple precursors, viz. KOH, $Ni(OH)_2$ (or NiO), and elemental S, instead of additional steps required to synthesize K_2S. This fully utilizes the advantage of the disproportionation of S in strong bases to form S^{2-}:

$$4S + 8OH^- \xrightarrow{\Delta} 3S^{2-} + SO_4^{2-} + 4H_2O \quad (1)$$

We observed that for reactions at 450 °C alone, phase selection was achieved by simply tuning the basicity and sulfur concentration, defined as [S] = mol(S)/[mol(LiOH) + mol(KOH)], since the S/Ni ratio was approximately maintained at 2.5:

$$2K^+ + 3Ni^{2+} + 4S^{2-} \xrightarrow{\Delta} K_2Ni_3S_4 \quad (2)$$

$$K^+ + 2Ni^{2+} + \frac{17}{8}S^{2-} + OH^- \xrightarrow{\Delta} KNi_2S_2 + \frac{1}{8}SO_4^{2-} + \frac{1}{2}H_2O \quad (3)$$

$$K^+ + 4Ni^{2+} + \frac{21}{8}S^{2-} + 5OH^- \xrightarrow{\Delta} KNi_4S_2 + \frac{5}{8}SO_4^{2-} + \frac{5}{2}H_2O \quad (4)$$

We have explained these reactions and the synthesis process in detail in Supporting Information (SI). The key observation is that the oxidation state of Ni in the ternary sulfide products tends to decrease with increasing basicity (increasing [KOH]) or decreasing [S] (Figure 1a−c). The reactions described in Figure 2a were subjected to rapid heating rate up to 450 °C at the rate of 20 °C/min. The reason for using such a high rate of heating was to minimize the dwell time at low temperatures because of the lower melting point of KOH compared to LiOH. The initial melt at a lower temperature was high in [KOH]. For example, for [KOH] = 0.7, the eutectic point is

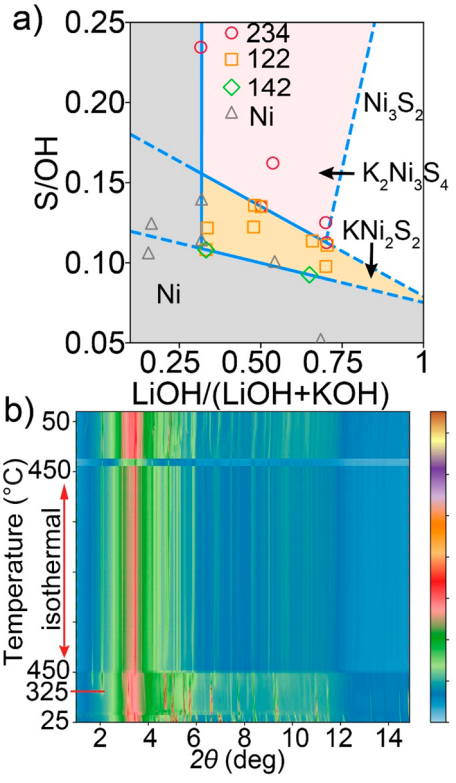

Figure 2. (a) Predominate phases as a function of [LiOH] and [S] and (b) panoramic synthesis of $K_2Ni_3S_4$ using *in situ* diffraction at high-resolution synchrotron source. The pink, orange, and gray areas in (a) depict phase regions for $K_2Ni_3S_4$, KNi_2S_2 and Ni, respectively. The phase region for KNi_4S_2 is very narrow and not distinguishable from Ni or KNi_2S_2, hence not shown in (a).

https://doi.org/10.1021/jacs.1c05107
J. Am. Chem. Soc. 2021, 143, 13646−13654

approximately 220 °C, whereas for [KOH] = 0.3, the mixture melts near 370 °C.[25] As shown in Figure 2a, for [S] = 0.1−0.125, [KOH] of 0.7, 0.5, and 0.3 generally favor KNi_4S_2 (Ni +0.75, Figure 1c), KNi_2S_2 (Ni +1.5, Figure 1b), and $K_2Ni_3S_4$ (Ni +2, Figure 1a), respectively. These results demonstrate the robustness and versatility of mixed KOH/LiOH melts as reaction media for the synthesis of complex chalcogenides. We begin by explaining the structure of the new ternary KNi_4S_2.

The crystal structure of KNi_4S_2 was determined by single-crystal X-ray diffraction (XRD) (Figure 1c and Table S2). It adopts a layered pseudo-square-net in the *Cmmm* space group with a = 3.6617(7) Å, b = 16.381(3) Å, and c = 3.6694(7) Å. Despite many similarities with the $ThCr_2Si_2$-type (122-type) structure adopted by KNi_2S_2 (Figure 1b and Table S3), the structure of KNi_4S_2 crystallizes in the $CeRe_2Si_2$ type.[26] In the 122-type KNi_2S_2, Ni and S form edge-sharing NiS_4 tetrahedra that extend to a square net. In contrast, there are only two neighboring S atoms in KNi_4S_2, forming bent S−Ni−S (Figure S6). The Ni(1)−S and Ni(2)−S bond distances were 2.230(4) and 2.215(3) Å, respectively, and their respective bond angles (S−Ni−S) were 110.4(2)° and 111.8(3)°, respectively. These are comparable to the bond distances of Ni−S (2.286(2) Å in KNi_2S_2) and the bond angles in the NiS_4 tetrahedron, i.e., 108.29(9)° and 111.86(17)°.

Because there are two Ni sheets sandwiched between the two S sheets, each Ni is surrounded by four neighboring Ni atoms in the plane to form a square planar structure, and four neighboring Ni atoms out of the plane to form a square pyramid structure (Figure S6). The Ni−Ni in-plane bond distance is 2.5921(4) Å, and the Ni(1)−Ni(1), Ni(1)−Ni(2), and Ni(2)−Ni(2) out-of-plane bond distances are 2.532(4), 2.558(3) and 2.578(4) Å, respectively. These bond distances are shorter than the Ni−Ni bond distance of 2.6780(4) Å in KNi_2S_2, but longer than those in metallic Ni ($Fm\bar{3}m$) (2.49 Å).[27] The in-plane Ni(2)−Ni(1)−Ni(2) and Ni(1)−Ni(2)−Ni(1) bond angles are 89.871(15)° and 90.111(16)°, respectively, because of the slight difference in the lattice constants a and c. These bond angles are slightly distorted from the right angle. However, even if each Ni layer forms a perfect square net without this distortion, the symmetry of the lattice would not be four-fold due to the glide plane between the two neighboring Ni sheets (Figure S6).

When [KOH] was decreased to 0.5 and 0.3, the products were KNi_2S_2 (Ni +1.5) and $K_2Ni_3S_4$ (Ni +2), respectively. We usually observed mixed phases for samples containing $K_2Ni_3S_4$. Based on our XRD analysis and elemental analysis with energy-dispersive X-ray spectroscopy (EDS) (described in detail in the SI section on polytypism in $K_2Ni_3S_4$), we attributed the secondary phase to a new hexagonal 2H-type $K_2Ni_3S_4$.[23,28] Therefore, we named the known $K_2Ni_3S_4$ (*Fddd*, 4O-type) and the 2H-type as α-$K_2Ni_3S_4$ and β-$K_2Ni_3S_4$, respectively.

These results demonstrated that with increasing flux solubility, more metastable compounds were favored. Our theoretical calculations show that the cohesive energy (enthalpy) for KNi_4S_2 is −0.470 eV/atom, whereas they are −0.869 and −1.016 eV/atom for KNi_2S_2 and α-$K_2Ni_3S_4$,[29] respectively (obtained from the Materials Project, which was also implemented using VASP for these calculations). The cohesive energy of KNi_4S_2 was even lower than that of α-$K_2Ni_3S_4$ + 5Ni (two formula units of KNi_4S_2) (−0.540 eV/atom). This indicated that KNi_4S_2 could not be prepared by traditional solid-state reactions. Indeed, our direct synthesis with Ni and polysulfides (16Ni + K_2S_3 + K_2S_5) at 400 °C produced only α-$K_2Ni_3S_4$ and Ni (Figure S7a). The heat treatment of KNi_4S_2 resulted in the decomposition of KNi_2S_2, Ni_3S_2, and Ni (Figure S7b,c). In addition to favoring metastable phases with increasing [KOH], it also tends to grow larger crystals because of its higher solubility. The crystals of $K_2Ni_3S_4$ grown with [KOH] = 0.3 are generally below 20−30 μm (Figure S8a), whereas when [KOH] increased to 0.5 and 0.7, the crystals of KNi_2S_2 and KNi_4S_2 can be as long as 200−300 μm (Figure S8b) and 1 mm (Figure S8c), respectively. The ability to grow single crystals of KNi_2S_2 (Table S3) for the first time, in this study, could provide suitable samples to study its exotic physical phenomena such as the alleged heavy fermion superconductivity.[20,21]

To fully illustrate the crystallization process, we carried out *in situ* panoramic synthesis with [KOH] = 0.3 (Figure 2b). Interestingly, we found that KNi_4S_2 was initially formed at 325 °C, but quickly disappeared or converted to the $K_2Ni_3S_4$ phase at 450 °C, which is the product of this reaction. To explain this, the heating process is taken into consideration. When the temperature of the mixture first reached the eutectic point at 220 °C, the [KOH] was approximately 0.7, instead of the intended value of 0.3, because excess LiOH was present in the solid form. With increasing temperature, more LiOH was dissolved and reduced the concentration of KOH, eventually leading to [KOH] = 0.3 at 370 °C. Considering the formation of the ternaries is almost instantaneous, the flux at lower temperature with high [KOH] (starting at [KOH] = 0.7 at the eutectic point) may initially favor KNi_4S_2. However, once the temperature reached 450 °C, the [KOH] decreased to the intended point of 0.3, which favored the formation of $K_2Ni_3S_4$. Thus, KNi_4S_2 was completely converted to $K_2Ni_3S_4$. Hence, we observed that at heating rates below 5 °C/min, KNi_4S_2 was more easily stabilized kinetically to afford a single phase without K vacancies (Table S1). We also carried out reactions at 350 and 400 °C. Although pure KNi_4S_2 can be prepared at 400 °C, the crystals are significantly smaller than those prepared at 450 °C. Interestingly, we detected a new kinetic phase for reactions conducted at 350 °C. Its composition is determined as "$K_4Ni_9S_{11}$" with EDS (Figure S2c) and it was indexed to a $P2/m$ space group with a = 7.16(1) Å, b = 13.98(2) Å, c = 5.232(9) Å, and β = 110.6(1)° using the indexing program DICVOL.[25] Our results exhibited that mixed hydroxide fluxes were capable of stabilizing kinetic products and control oxidation states via tunable solubility.

Oxidation State Control. We could select different sulfide phases of Ni with oxidation states of +0.75−1, +1.5, and +2 in a one-pot reaction. This is quite remarkable, as even molecular species of Ni(I) complexes are rare. In addition, their pathways are usually multi-step involving oxidation or reduction of a Ni(0) or Ni(II) precursor, respectively, whereas the reaction type we describe here offers a direct synthesis.[30] This is quite intriguing because the synthesis of complex precursors is not required. This can significantly reduce the number of synthetic variables. We attribute this feature to the acid/base nature of the mixed hydroxide flux, similar to the aqueous solution. zur Loye et al.[5] compared the similarities between molten hydroxides and water and proposed a self-dissociation similar to H_2O:

$$2OH^- \leftrightarrow H_2O + O^{2-} \quad (5)$$

where H_2O and O^{2-} serve as the acid and base, respectively. The dissociation constant $K_d = [H_2O][O^{2-}]$ is an indicator of the basicity of different alkali bases. At 400 °C, the K_d of KOH

https://doi.org/10.1021/jacs.1c05107
J. Am. Chem. Soc. 2021, 143, 13646−13654

is about 7 orders of magnitude smaller than the K_d of LiOH, indicating a much weaker acid or stronger base. Thus, when KOH and LiOH are mixed, we can create a pK_d window of 7, which is sufficient to tune the basicity of the melt by varying the KOH/LiOH ratio.

Despite the high effectiveness of all the common fluxes in materials discovery, they do not offer an easy way to control the oxidation state of other metals in the final products. Often, a specific oxidation state is important for obtaining materials with the desired properties. For example, the need for precise oxidation state control is crucial for Fe-based superconductors. KFe_2Se_2 (nominal $Fe^{+1.5}$) was first found to be a 35 K filamentary superconductor;[31] however, the superconducting phase $K_{1-x}Fe_{2-y}Se_2$ (actual $Fe^{+1.75-1.8}$) was not identified until a more detailed study with single crystal diffraction by Shoemaker et al. due to the many impurity phases involved in its synthesis.[32] Hence, Clarke et al. followed an alternative pathway to precisely control the oxidation state using Birch reduction of FeSe with alkali metals in liquid ammonia and obtained bulk superconductors at 43 K.[33,34] Similarly, they also found that the optimal doping level for Fe is 0.2−0.25 e^- ($Fe^{+1.75-1.8}$). Our findings provide a facile pathway for oxidation state control using mixed hydroxide fluxes.

Binary Ni_2S by Deintercalation of KNi_4S_2. We observed that when using a flux composition that favored a Ni oxidation state higher than +0.75 (e.g., [KOH] = 0.5−0.7), a K vacancy-ordered superlattice (with a 3-fold larger unit cell volume than KNi_4S_2) with a composition of $K_{1-x}Ni_4S_2$ (x = 0.325) was formed (Table S4). This is essentially a partially K-deintercalated phase of KNi_4S_2 (Figure 3a), where the Ni atoms have a slightly higher oxidation state. This indicates that full removal of K ions might be possible with oxidative deintercalation. This was accomplished using KNi_4S_2 as a template precursor in the reaction with a flux that favors $Ni^{+1-1.2}$ by using [KOH] = 0.5−0.7. This resulted in a new binary isostructural compound, Ni_2S (Figure 3b). While it is possible that the binary Ni_2S is a product of the topochemical deintercalation of K, it is also possible that KNi_4S_2 re-dissolved and precipitated as Ni_2S. The powder X-ray diffraction (PXRD) pattern shows an unidentified phase for the as-recovered product with a 1.6 Å smaller layered spacing (~6.6 Å, Figure 3d) compared to 8.19 Å of KNi_4S_2. Similar K-deintercalation from KCo_2Se_2 to CoSe also resulted in a reduction in the layered spacing of about 1.6 Å (from 6.92 to 5.33 Å).[35] In addition, EDS shows no sign of K lines with a Ni:S ratio of about 2:1 (Figure S9a). Therefore, this new compound could be a binary of Ni_2S isostructural to the Ni_2S layers in KNi_4S_2.

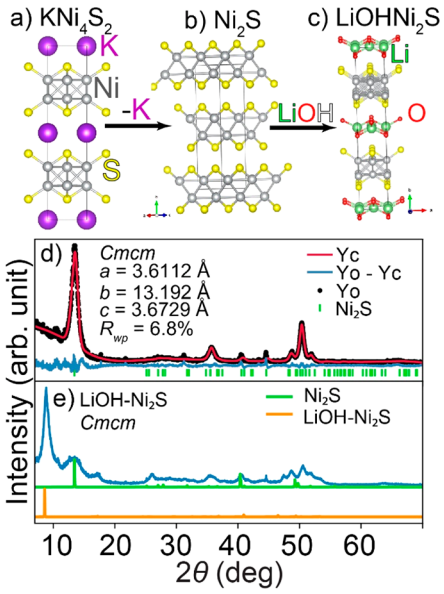

Figure 3. Topochemical manipulation of (a) KNi_4S_2 to form (b) Ni_2S and (c) LiOH-intercalated Ni_2S. The powder X-ray diffraction patterns (PXRD) collected with laboratory source of (d) Ni_2S and (e) LiOH-intercalated Ni_2S show successful deintercalation and ion-exchange to Ni_2S and LiOH−Ni_2S, respectively. Corresponding EDS analysis of (d) Ni_2S showed the absence of K in this compound (Figure S9a), thus proving successful deintercalation. Simulated peaks for Ni_2S and LiOH−Ni_2S matches major peaks in (e), indicating an incomplete conversion from Ni_2S to LiOH−Ni_2S.

Upon deintercalation of K, every other layer of Ni_2S should shift by half of the unit cell of a or c to avoid direct overlap between the two neighboring S^{2-} layers, which is also seen in CoSe after deintercalation.[35] Thus, the mirror planes parallel to the ac plane become glide planes, reducing the symmetry from *Cmmm* to *Cmcm*. This new structure fits well with the PXRD data shown in Figure 3d.

In addition to Ni_2S, an unknown phase with a larger layered spacing (~10.3 Å, Figure 3e) occurred when [KOH] was close to 0.5. We were unable to obtain a pure phase without the complete removal of Ni_2S. This new phase also showed a Ni/S ratio of 2:1 but contained a small amount of K; thus, an overall stoichiometric ratio of $K_{0.2}Ni_2S$. However, if the compound is an incomplete deintercalated KNi_4S_2, its layered spacing would not be ~2 Å larger than that of KNi_4S_2. Therefore, it is likely that LiOH, which also adopts a van der Waals square lattice, is inserted between Ni_2S to cause a similarly large lattice expansion. We proposed a structure (Figure 3c) in the *Cmcm* space group that was verified with *Platon*. Although the data quality of the PXRD data is not adequate for Rietveld refinement, the intercalation chemistry and lattice expansion are quite similar to those of LiOH-intercalated FeSe.[36,37] Therefore, it is very likely that this new compound is LiOH-intercalated Ni_2S.

Since we do not have single-crystal data for these topochemically formed compounds, we confirmed their pseudo-square lattice by electron diffraction (Figure 4a,b). These results are in agreement with our PXRD data and suggest that the conversion from KNi_4S_2 to Ni_2S and LiOH-Ni_2S is indeed topotactic. Interestingly, from high-resolution transmission electron microscopy (HR-TEM) image of edge-on LiOH−Ni_2S, we observed random stacking faults, as illustrated in Figure 4c. The average distance between the usual lattice fringes (Figure 4d) are 0.52 nm (about half the lattice parameter c of LiOH-Ni_2S). However, a stacking fault or lattice distortion shown in HR-TEM corresponds to a disruption of the usual periodic distance, which was reduced to 0.43 nm (about half the distance of the layered spacing in KNi_4S_2). This suggests that the topotactic conversion from KNi_4S_2 to LiOH-Ni_2S is incomplete because of the shorter lattice spacing and lattice distortion originated from unchanged KNi_4S_2. This is corroborated by X-ray photoelectron spectroscopy (XPS) analysis, as the spectrum of K-2p is observed for LiOH-Ni_2S (Figure S11), whereas it was absent for Ni_2S (Figure S13)

XAS Analysis. We examined the electron density on Ni using X-ray absorption spectroscopy (XAS) at the advanced photon source (APS) and X-ray photoelectron spectroscopy

https://doi.org/10.1021/jacs.1c05107
J. Am. Chem. Soc. 2021, 143, 13646−13654

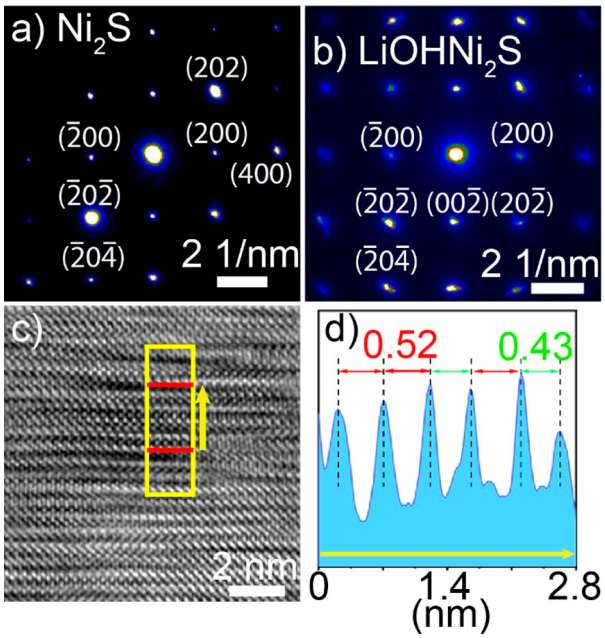

Figure 4. Electron diffraction patterns of (a) Ni_2S and (b) LiOH−Ni_2S along the zone axis of [010] showing pseudo-square lattice, (c) high-resolution transmission electron microcopy (HR-TEM) image of LiOH−Ni_2S, and (d) distance analysis for the lattice fringe between the two red lines enclosed within the yellow box shown in (c). The direction of the yellow arrow in (c) corresponds to the direction of the distance shown in (d).

(XPS) because KNi_4S_2 and Ni_2S exhibit unusual Ni oxidation states (XPS section in the SI). Specifically, Ni K-edge X-ray absorption near-edge structure spectroscopy (XANES) and extended X-ray absorption fine structure spectroscopy (EXAFS) were used to assess the approximate oxidation state of Ni and the coordination environment around the Ni absorber, respectively.

Figure 5a depicts the XANES spectra of the Ni^0 foil reference, Ni_2S, KNi_2S_2, and KNi_4S_2. Using the midpoint of the 1s→3d transition (effective energy at normalized intensity ∼0.5), we observed X-ray energies of 8332.3, 8335.2, 8335.8, and 8338.2 (±0.2) eV for Ni^0, Ni_2S, KNi_4S_2, and KNi_2S_2, respectively. The total energy offset from Ni^0 for KNi_4S_2 and Ni_2S (∼3 eV) is approximately half of that for KNi_2S_2 (∼6 eV). This is in agreement with the expected oxidation state of KNi_4S_2 of 0.75, halfway between Ni^0 and KNi_2S_2.

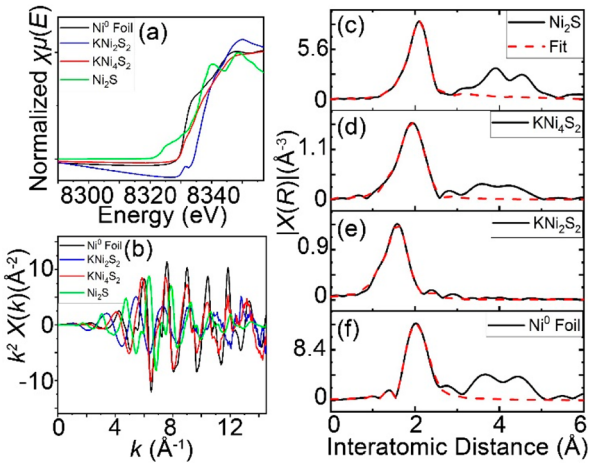

Figure 5. XAS data of (a) Ni K-edge X-ray absorption near-edge structure (XANES), (b) correlation of Ni, 122, 142 and Ni_2S, interatomic distance of (c) Ni_2S, (d) KNi_4S_2, (e) KNi_2S_2, and (f) Ni foil.

The reverse Fourier-transform EXAFS spectra are shown in Figure 5b. To assess the local coordination environment in the first coordination shell around the Ni atom, Ni K-edge EXAFS (real part of the k^2-weighted reverse FT EXAFS) analysis was performed (Figure 5c−f). The Ni−S scattering pathway in KNi_4S_2 and Ni_2S could not be decoupled from the Ni−Ni scattering pathway due to the statistical broadening of the first coordination shell at the interatomic distance (R) range of $1 < R < 3$ Å. To generate local structural parameters, we maintained the coordination numbers (CN) for the dominant Ni−Ni and Ni−S scatters at 4 and 2, respectively. Therefore, in this approach, only the structural disorder factor (Debye−Waller factor), σ^2, and interatomic (bond) distances, R, were allowed to vary. Hence, the fitted interatomic distances are not an accurate reflection of the actual values. Therefore, we only compared the trends qualitatively.

Using the fitting scheme stated above, we fit the first coordination shell fairly well for Ni_2S, KNi_4S_2, KNi_2S_2, and Ni (Figure 5c−f). The average length of scattering pathways for both Ni_2S and KNi_4S_2 shows a significant shift toward higher values (0.3−0.4 Å) compared to KNi_2S_2. This is a result of the coupling between the Ni−Ni and Ni−S pathways in Ni_2S and KNi_4S_2. From the crystal structure of KNi_4S_2, the first coordination shell for each Ni consists of two S atoms at about 2.22 Å and eight Ni atoms between 2.53−2.58 Å. Therefore, the average scattering length of KNi_4S_2 was higher than that of KNi_2S_2. In comparison, the Ni−Ni distance in KNi_2S_2 is larger (2.6780(4) Å), and there are only four nearest neighbors. Hence, the Ni−Ni scattering of the first coordination shell in KNi_2S_2 is depicted as a shoulder after the major peak of the Ni−S scattering pathways (Figure 5e), which is similar to that of KNi_2Se_2.[38] The Ni−Ni scattering pathways for the second coordination shell at $R = 3-5$ Å is absent in KNi_2S_2 but significant for the Ni^0 reference foil, Ni_2S, and KNi_4S_2. This is in agreement with our structural models for KNi_4S_2 and Ni_2S, where the two neighboring Ni layers provide Ni−Ni interactions similar to those in metallic Ni.

***Ab Initio* Calculations.** We performed density functional theory (DFT) calculations for both KNi_4S_2 and Ni_2S. The structural model for Ni_2S is based on the lattice constants obtained from the PXRD data shown in Figure 3d. The atomic coordinates were estimated to retain the Ni−Ni and Ni−S bond distances, similar to that observed in KNi_4S_2. The structural information for both compounds was converted to $P1$ symmetry, and both lattice constants and atomic coordinates were fully relaxed because rotational symmetry is not employed by the VASP code. The results of the relaxed cells are shown in Tables S5 and S6 for KNi_4S_2 and Ni_2S, respectively. Their structural models in the space group of $P1$ were then validated with *Platon*,[39] which suggested space groups of *Cmmm* and *Cmcm* for KNi_4S_2 and Ni_2S, respectively. The relaxed lattice constants for KNi_4S_2 are comparable with the experimental data shown in Table S2, whereas for Ni_2S the layered spacing is ∼0.3 Å larger than the value obtained from refinement of the PXRD data (6.95 Å vs 6.60 Å). This is common for DFT calculations, as they often overestimate the lattice constants, especially for van der Waals compounds.

https://doi.org/10.1021/jacs.1c05107
J. Am. Chem. Soc. 2021, 143, 13646−13654

The electronic structures of both compounds were calculated based on the relaxed cells shown in Tables S5 and S6. To understand the bonding in KNi_4S_2 and Ni_2S, we performed calculations for crystal orbital Hamiltonian population (COHP) analysis using the LOBSTER code.[40−42] The bonding and antibonding interactions were plotted as positive and negative states, respectively, for KNi_4S_2 and Ni_2S (Figure 6a,b). KNi_4S_2 exhibits strong antibonding characteristics for both Ni−S and Ni−Ni interactions at the Fermi level. The bonding interactions for Ni−S and Ni−Ni are 4 and 2 eV, respectively, below the Fermi level. In comparison, the bonding orbitals are 1.5 eV below the Fermi level in the 122-type KNi_2Se_2 ($Ni^{+1.5}$), leaving an unfilled $d_{x^2-y^2}$ orbital.[43] Our partial Density of State (pDOS) calculations show that the dominant Ni d-orbital character close to the Fermi level is $d_{x^2-y^2}$ (Figure 6d) and most of the states for its Ni d-orbitals are below the Fermi level. This suggests a rather high electron filling level for KNi_4S_2, which is consistent with the electron-rich nature of Ni in KNi_4S_2. Similarly, Ni_2S also exhibits strong antibonding characteristics at the Fermi level (Figure 6b), which exactly lands on the peak of the Ni-$d_{x^2-y^2}$ orbital (Figure 6c). Since the Fermi level of KNi_4S_2 is beyond this peak, the electron filling in Ni_2S is less than that in KNi_4S_2.

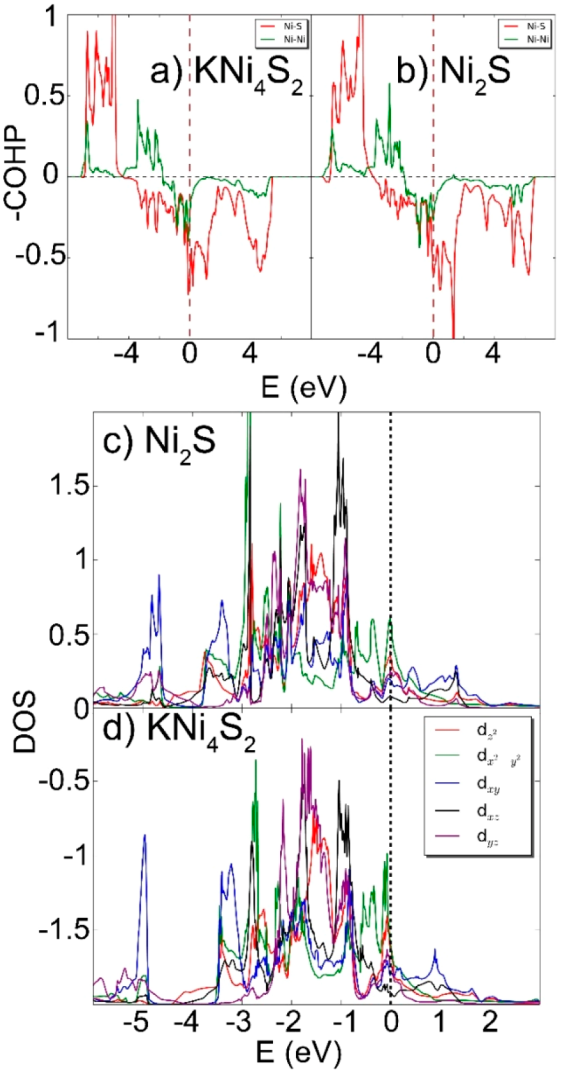

Figure 6. Crystal orbital Hamilton population (COHP) of (a) KNi_4S_2 and (b) Ni_2S. Partial density of state (pDOS) for 3d orbitals of Ni for (c) Ni_2S and (d) KNi_4S_2. Positive and negative states of COHP depict bonding and antibonding interactions, respectively.

The fairly large electronic states at the Fermi level for both KNi_4S_2 and Ni_2S (Figure 6c,d) may lead to possible electronic instability such as ferromagnetism, known as Stoner's criterion for ferromagnetism.[44] Thus, we found that both compounds show itinerant ferromagnetism, which will be reported in a subsequent study. Interestingly, this is similar to many 122-type ACo_2Q_2 (A = K, Rb, Cs, and Sr; Q = S, Se, and As), such as KCo_2Se_2, $RbCo_2Se_2$, and $SrCo_2As_2$.[45−48] Birgeneau et al.[48] suggest that itinerant ferromagnetism in this type of compounds is induced by a large flat-band close to the Fermi level (within 0.1 eV). Our band structure calculations identify a flat-band 0.05 eV below the Fermi level from for KNi_4S_2 (Figure 7a) and a flat-band at the Fermi level for Ni_2S (Figure 7b) from X-M-Γ. In comparison with the pDOS plots (Figure 6c,d), the major orbital characters for these two bands are both Ni-$d_{x^2-y^2}$. Interestingly, a recent angle-resolved photoemission spectroscopy (ARPES) study combined with DFT calculations found that the major orbital character of the flat-band in $RbCo_2Se_2$ is also $d_{x^2-y^2}$.[48] Since the flatbands of the 122-type Fe-based superconductors and ANi_2Q_2 superconductors are much farther away from the Fermi level,[43] it is suggested that the flat-band could be shifted away from the Fermi level by tuning the electron filling. This shift can lead to the suppression of this itinerant ferromagnetism and possible superconductivity.[48]

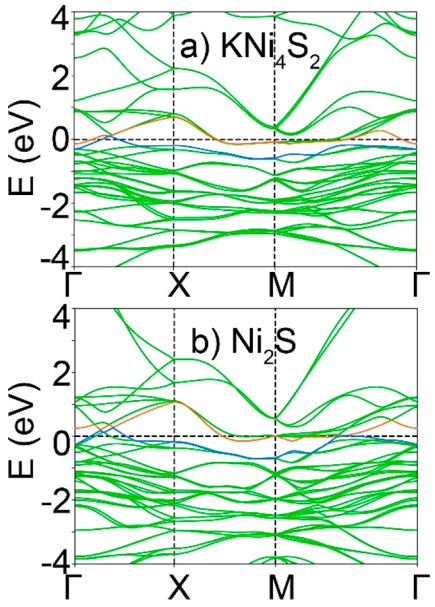

Figure 7. Density functional theory (DFT) calculations depicting the band structures of (a) KNi_4S_2 and (b) Ni_2S. The two bands close to the Fermi level in both (a) and (b) are highlighted with blue and orange colors.

We also noticed an interesting change in the band structure after the deintercalation of KNi_4S_2. We highlighted two bands close to the Fermi level with blue and orange colors (Figure 7). In KNi_4S_2, the blue and orange bands are connected via one point from Γ-X. After deintercalation, a single point becomes a pair of cones. When compared to Dirac points in topological semimetals,[49] they are above the Fermi level. This interesting feature requires further investigation in future studies.

https://doi.org/10.1021/jacs.1c05107
J. Am. Chem. Soc. 2021, 143, 13646−13654

CONCLUSIONS

In this study, we employed molten salts beyond their typical empirical use in exploratory synthesis and have gleaned the reaction trends to gain control of the phase section in the K−Ni−S system. Using a mixed KOH/LiOH flux as a high-temperature solvent, we were able to obtain all known ternaries of K−Ni−S. In addition, by rationally adjusting the basicity (solubility) of the solution, we could precisely control the oxidation states of Ni, which led to the synthesis of a new layered compound, KNi_4S_2. Furthermore, our results indicated that by increasing the solubility of the flux, the reaction pathway shifted toward the formation of more complex and metastable phases. Thus, using mixed fluxes with tunable solubility could be an effective design strategy for the discovery of novel materials. For the Ni−S system alone, we readily uncovered other novel phases when LiOH is mixed with NaOH, RbOH, and CsOH, which will be reported in the future. While many synthesis reactions have frequently been rationalized on "chemical principles" (e.g., basicity, hard/soft concepts), a truly mechanistic approach to guiding the predictive creation of targeted phases lies just out of reach due to their complexity or metastability. The current study highlights the opportunity for a rules-based framework of "control in materials synthesis" that will inspire future efforts in the science of synthesis.

ASSOCIATED CONTENT

Supporting Information

The Supporting Information is available free of charge at https://pubs.acs.org/doi/10.1021/jacs.1c05107.

Theoretical methods of DFT calculations and experimental methods including diffraction techniques, electron microscopy, EDS for elemental analysis, XANES, EXAFS, and XPS, including Figures S1−S13 and Tables S1−S6 (PDF)

Accession Codes

CCDC 2088104−2088106 contain the supplementary crystallographic data for this paper. These data can be obtained free of charge via www.ccdc.cam.ac.uk/data_request/cif, or by emailing data_request@ccdc.cam.ac.uk, or by contacting The Cambridge Crystallographic Data Centre, 12 Union Road, Cambridge CB2 1EZ, UK; fax: +44 1223 336033.

AUTHOR INFORMATION

Corresponding Author

Mercouri G. Kanatzidis − *Materials Science Division, Argonne National Laboratory, Lemont, Illinois 60439, United States; Department of Chemistry, Northwestern University, Evanston, Illinois 60208, United States;* orcid.org/0000-0003-2037-4168; Email: m-kanatzidis@northwestern.edu

Authors

Xiuquan Zhou − *Materials Science Division, Argonne National Laboratory, Lemont, Illinois 60439, United States;* orcid.org/0000-0002-1361-3880

David J. Mandia − *Materials Science Division, Argonne National Laboratory, Lemont, Illinois 60439, United States;* orcid.org/0000-0003-0325-3612

Hyowon Park − *Department of Physics, University of Illinois at Chicago, Chicago, Illinois 60607, United States*

Mahalingam Balasubramanian − *X-ray Science Division, Advanced Photon Source, Argonne National Laboratory, Argonne, Illinois 60439, United States*

Lei Yu − *Chemical Sciences and Engineering Division, Argonne National Laboratory, Lemont, Illinois 60439, United States*

Jianguo Wen − *Nanoscience and Technology Division, Argonne National Laboratory, Lemont, Illinois 60439, United States;* orcid.org/0000-0002-3755-0044

Andrey Yakovenko − *X-ray Science Division, Advanced Photon Source, Lemont, Illinois 60439, United States*

Duck Young Chung − *Materials Science Division, Argonne National Laboratory, Lemont, Illinois 60439, United States*

Complete contact information is available at: https://pubs.acs.org/10.1021/jacs.1c05107

Notes

The authors declare no competing financial interest.

ACKNOWLEDGMENTS

This work was supported by the U.S. Department of Energy, Office of Science, Basic Energy Sciences, Materials Sciences, and the Engineering Division. EDS/SEM and TEM/EELS analyses were carried out at the Center for Nanoscale Materials (CNM), which is the Office of Science user facilities supported by the U.S. Department of Energy, Office of Science, Office of Basic Energy Sciences, under Contract No. DE-AC02-06CH11357. Work at the 17-BM and 20-BM beamlines at the Advanced Photon Source (APS) at Argonne National Laboratory was supported by the U.S. Department of Energy, Office of Science, Office of Basic Energy Sciences under contract No. DE-AC02-06CH11357. H. Park was supported by the U.S. Department of Energy, Office of Science, Basic Energy Sciences, Materials Sciences, and Engineering Division. H.P. acknowledges the computing resources provided by Bebop, a high-performance computing cluster operated by the Laboratory Computing Resource Center at Argonne National Laboratory.

REFERENCES

(1) Do, J.; Yun, H. A new one-dimensional quaternary metal thiophosphate: synthesis and structure of KNb2PS10. *Inorg. Chem.* **1996**, *35*, 3729.

(2) McCarthy, T. J.; Kanatzidis, M. G. Use of molten alkali-metal polythiophosphate fluxes for synthesis at intermediate temperatures. Isolation and structural characterization of $ABiP_2S_7$ (A= K, Rb). *Chem. Mater.* **1993**, *5*, 1061.

(3) Cody, J.; Mansuetto, M.; Chien, S.; Ibers, J. A. In *Mater. Sci. Forum*; Trans Tech Publ: 1994; Vol. *152*, p 35.

(4) Kanatzidis, M. G. New directions in synthetic solid state chemistry: chalcophosphate salt fluxes for discovery of new multinary solids. *Curr. Opin. Solid State Mater. Sci.* **1997**, *2*, 139.

(5) Mugavero, S. J., III; Gemmill, W. R.; Roof, I. P.; zur Loye, H.-C. Materials discovery by crystal growth: Lanthanide metal containing oxides of the platinum group metals (Ru, Os, Ir, Rh, Pd, Pt) from molten alkali metal hydroxides. *J. Solid State Chem.* **2009**, *182*, 1950.

(6) Bugaris, D. E.; zur Loye, H. C. Materials discovery by flux crystal growth: quaternary and higher order oxides. *Angew. Chem., Int. Ed.* **2012**, *51*, 3780.

(7) Kanatzidis, M. G. Discovery-Synthesis, Design, and Prediction of Chalcogenide Phases. *Inorg. Chem.* **2017**, *56*, 3158.

(8) Klepov, V. V.; Juillerat, C. A.; Pace, K. A.; Morrison, G.; zur Loye, H.-C. Soft" Alkali Bromide and Iodide Fluxes for Crystal Growth. *Front. Chem.* **2020**, *8*, 518.

(9) Vasquez, G.; Huq, A.; Latturner, S. E. In Situ Neutron Diffraction Studies of the Metal Flux Growth of Ba/Yb/Mg/Si Intermetallics. *Inorg. Chem.* **2019**, *58*, 8111.
(10) Usman, M.; Smith, M. D.; Klepov, V. V.; zur Loye, H.-C. One-Dimensional Quaternary and Penternary Alkali Rare Earth Thiophosphates Obtained via Alkali Halide Flux Crystal Growth. *Cryst. Growth Des.* **2019**, *19*, 5648.
(11) Hara, H.; Adachi, S.; Matsumoto, R.; Yamashita, A.; Takeya, H.; Takano, Y. Single Crystal Growth of Cuprate Superconductor $(Lu_{0.8}Nd_{0.2})Ba_2Cu_4O_8$ by KOH Flux Method. *J. Phys. Soc. Jpn.* **2018**, *87*, 123705.
(12) Shoemaker, D. P.; Chung, D. Y.; Mitchell, J.; Bray, T. H.; Soderholm, L.; Chupas, P. J.; Kanatzidis, M. G. Understanding fluxes as media for directed synthesis: In situ local structure of molten potassium polysulfides. *J. Am. Chem. Soc.* **2012**, *134*, 9456.
(13) Shoemaker, D. P.; Hu, Y.-J.; Chung, D. Y.; Halder, G. J.; Chupas, P. J.; Soderholm, L.; Mitchell, J.; Kanatzidis, M. G. In situ studies of a platform for metastable inorganic crystal growth and materials discovery. *Proc. Natl. Acad. Sci. U. S. A.* **2014**, *111*, 10922.
(14) McClain, R.; Malliakas, C. D.; Shen, J.; He, J.; Wolverton, C.; González, G. B.; Kanatzidis, M. G. Mechanistic insight of $KBiQ_2$ (Q = S, Se) using panoramic synthesis towards synthesis-by-design. *Chemical Science* **2021**, *12*, 1378.
(15) Abeysinghe, D.; Huq, A.; Yeon, J.; Smith, M. D.; zur Loye, H.-C. In Situ Neutron Diffraction Studies of the Flux Crystal Growth of the Reduced Molybdates $La_4Mo_2O_{11}$ and $Ce_4Mo_2O_{11}$: Revealing Unexpected Mixed-Valent Transient Intermediates and Determining the Sequence of Events during Crystal Growth. *Chem. Mater.* **2018**, *30*, 1187.
(16) Haynes, A. S.; Stoumpos, C. C.; Chen, H.; Chica, D.; Kanatzidis, M. G. Panoramic Synthesis as an Effective Materials Discovery Tool: The System Cs/Sn/P/Se as a Test Case. *J. Am. Chem. Soc.* **2017**, *139*, 10814.
(17) Hsu, F.-C.; Luo, J.-Y.; Yeh, K.-W.; Chen, T.-K.; Huang, T.-W.; Wu, P. M.; Lee, Y.-C.; Huang, Y.-L.; Chu, Y.-Y.; Yan, D.-C.; Wu, M.-K. Superconductivity in the PbO-type structure α-FeSe. *Proc. Natl. Acad. Sci. U. S. A.* **2008**, *105*, 14262.
(18) Guo, J.; Jin, S.; Wang, G.; Wang, S.; Zhu, K.; Zhou, T.; He, M.; Chen, X. Superconductivity in the iron selenide $K_xFe_2Se_2$ ($0 \leq x \leq 1.0$). *Phys. Rev. B: Condens. Matter Mater. Phys.* **2010**, *82*, 180520.
(19) Wang, H.; Dong, C.; Mao, Q.; Khan, R.; Zhou, X.; Li, C.; Chen, B.; Yang, J.; Su, Q.; Fang, M. Multiband superconductivity of heavy electrons in a $TlNi_2Se_2$ single crystal. *Phys. Rev. Lett.* **2013**, *111*, 207001.
(20) Neilson, J. R.; McQueen, T. M.; Llobet, A.; Wen, J.; Suchomel, M. R. Charge density wave fluctuations, heavy electrons, and superconductivity in KNi_2S_2. *Phys. Rev. B: Condens. Matter Mater. Phys.* **2013**, *87*, 045124.
(21) Neilson, J. R.; Llobet, A.; Stier, A. V.; Wu, L.; Wen, J.; Tao, J.; Zhu, Y.; Tesanovic, Z. B.; Armitage, N.; McQueen, T. M. Mixed-valence-driven heavy-fermion behavior and superconductivity in KNi_2Se_2. *Phys. Rev. B: Condens. Matter Mater. Phys.* **2012**, *86*, 054512.
(22) McQueen, T. M.; Huang, Q.; Ksenofontov, V.; Felser, C.; Xu, Q.; Zandbergen, H.; Hor, Y. S.; Allred, J.; Williams, A. J.; Qu, D.; et al. Extreme sensitivity of superconductivity to stoichiometry in $Fe_{1+\delta}Se$. *Phys. Rev. B: Condens. Matter Mater. Phys.* **2009**, *79*, 014522.
(23) Bronger, W.; Rennau, R.; Schmitz, D. Schichtstrukturen ternärer Chalkogenide $A_2M_3X_4$ (A ≙ K, Rb, Cs; M ≙ Ni, Pd, Pt; X ≙ S, Se). *Z. Anorg. Allg. Chem.* **1991**, *597*, 27.
(24) Neilson, J. R.; McQueen, T. M.; Llobet, A.; Wen, J.; Suchomel, M. R. Charge density wave fluctuations, heavy electrons, and superconductivity in KNi_2S_2. *Phys. Rev. B: Condens. Matter Mater. Phys.* **2013**, *87*, 045124.
(25) Bale, C. W.; Pelton, A. D. Coupled phase diagram and thermodynamic analysis of the 18 binary systems formed among Li_2CO_3, K_2CO_3,Na_2CO_3, LiOH, KOH, NaOH, Li_2SO_4, K_2SO_4 and Na_2SO_4. *CALPHAD: Comput. Coupling Phase Diagrams Thermochem.* **1982**, *6*, 255.
(26) Bodak, O.; Gladyshevskij, E.; Pecharskij, V. Crystal structure of $CeRe_4Si_2$ compound. *Kristallografiya* **1977**, *22*, 178.
(27) Jørgensen, J. E.; Smith, R. I. On the compression mechanism of FeF_3. *Acta Crystallogr., Sect. B: Struct. Sci.* **2006**, *62*, 987.
(28) Bronger, W.; Rennau, R.; Schmitz, D. Die Kristallstrukturen von $Cs_2Ni_3S_4$. *Z. Kristallogr. - Cryst. Mater.* **1988**, *183*, 201.
(29) Jain, A.; Ong, S. P.; Hautier, G.; Chen, W.; Richards, W. D.; Dacek, S.; Cholia, S.; Gunter, D.; Skinner, D.; Ceder, G.; Persson, K. A. Commentary: The Materials Project: A materials genome approach to accelerating materials innovation. *APL Mater.* **2013**, *1*, 011002.
(30) Lin, C.-Y.; Power, P. P. Complexes of Ni(i): a "rare" oxidation state of growing importance. *Chem. Soc. Rev.* **2017**, *46*, 5347.
(31) Guo, J.; Jin, S.; Wang, G.; Wang, S.; Zhu, K.; Zhou, T.; He, M.; Chen, X. Superconductivity in the iron selenide $K_xFe_2Se_2$. *Phys. Rev. B: Condens. Matter Mater. Phys.* **2010**, *82*, 180520.
(32) Shoemaker, D. P.; Chung, D. Y.; Claus, H.; Francisco, M. C.; Avci, S.; Llobet, A.; Kanatzidis, M. G. Phase relations in $K_xFe_{2-y}Se_2$ and the structure of superconducting $K_xFe_2Se_2$ via high-resolution synchrotron diffraction. *Phys. Rev. B: Condens. Matter Mater. Phys.* **2012**, *86*, 184511.
(33) Burrard-Lucas, M.; Free, D. G.; Sedlmaier, S. J.; Wright, J. D.; Cassidy, S. J.; Hara, Y.; Corkett, A. J.; Lancaster, T.; Baker, P. J.; Blundell, S. J.; Clarke, S. J. Enhancement of the superconducting transition temperature of FeSe by intercalation of a molecular spacer layer. *Nat. Mater.* **2013**, *12*, 15.
(34) Sedlmaier, S. J.; Cassidy, S. J.; Morris, R. G.; Drakopoulos, M.; Reinhard, C.; Moorhouse, S. J.; O'Hare, D.; Manuel, P.; Khalyavin, D.; Clarke, S. J. Ammonia-rich high-temperature superconducting intercalates of iron selenide revealed through time-resolved in situ x-ray and neutron diffraction. *J. Am. Chem. Soc.* **2014**, *136*, 630.
(35) Zhou, X.; Wilfong, B.; Vivanco, H.; Paglione, J.; Brown, C. M.; Rodriguez, E. E. Metastable layered cobalt chalcogenides from topochemical deintercalation. *J. Am. Chem. Soc.* **2016**, *138*, 16432.
(36) Lu, X.; Wang, N.; Zhang, G.; Luo, X.; Ma, Z.; Lei, B.; Huang, F.; Chen, X. Superconductivity in $LiFeO_2Fe_2Se_2$ with anti-PbO-type spacer layers. *Phys. Rev. B: Condens. Matter Mater. Phys.* **2014**, *89*, 020507.
(37) Zhou, X.; Borg, C. K.; Lynn, J. W.; Saha, S. R.; Paglione, J.; Rodriguez, E. E. The preparation and phase diagrams of $(^7Li_{1-x}Fe_xOD)$ FeSe and $(Li_{1-x}Fe_xOH)$FeSe superconductors. *J. Mater. Chem. C* **2016**, *4*, 3934.
(38) Neilson, J. R.; Drichko, N.; Llobet, A.; Balasubramanian, M.; Suchomel, M. R.; McQueen, T. M. Local increase of symmetry on cooling in KNi_2Se_2 arXiv Preprint 1310.6828, Oct 25, 2013 (https://arxiv.org/abs/1310.6828).
(39) Spek, A. Single-crystal structure validation with the program PLATON. *J. Appl. Crystallogr.* **2003**, *36*, 7.
(40) Maintz, S.; Deringer, V. L.; Tchougréeff, A. L.; Dronskowski, R. Analytic projection from plane-wave and PAW wavefunctions and application to chemical-bonding analysis in solids. *J. Comput. Chem.* **2013**, *34*, 2557.
(41) Deringer, V. L.; Tchougréeff, A. L.; Dronskowski, R. Crystal Orbital Hamilton Population (COHP) Analysis As Projected from Plane-Wave Basis Sets. *J. Phys. Chem. A* **2011**, *115*, 5461.
(42) Dronskowski, R.; Bloechl, P. E. Crystal orbital Hamilton populations (COHP): energy-resolved visualization of chemical bonding in solids based on density-functional calculations. *J. Phys. Chem.* **1993**, *97*, 8617.
(43) Neilson, J. R.; McQueen, T. M. Bonding, Ion Mobility, and Rate-Limiting Steps in Deintercalation Reactions with $ThCr_2Si_2$-type KNi_2Se_2. *J. Am. Chem. Soc.* **2012**, *134*, 7750.
(44) Stoner, E. C. Collective electron ferronmagnetism. *Proc. R. Soc. London, Ser. A* **1938**, *165*, 372.
(45) Li, Y.; Yin, Z.; Liu, Z.; Wang, W.; Xu, Z.; Song, Y.; Tian, L.; Huang, Y.; Shen, D.; Abernathy, D. L.; Niedziela, J. L.; Ewings, R. A.; Perring, T. G.; Pajerowski, D. M.; Matsuda, M.; Bourges, P.; Mechthild, E.; Su, Y.; Dai, P. Coexistence of Ferromagnetic and Stripe Antiferromagnetic Spin Fluctuations in $SrCo_2As_2$. *Phys. Rev. Lett.* **2019**, *122*, 117204.

https://doi.org/10.1021/jacs.1c05107
J. Am. Chem. Soc. 2021, 143, 13646−13654

(46) Liu, Z.; Zhao, Y.; Li, Y.; Jia, L.; Cai, Y.; Zhou, S.; Xia, T.; Büchner, B.; Borisenko, S.; Wang, S. Orbital characters and electronic correlations in KCo_2Se_2. *J. Phys.: Condens. Matter* **2015**, *27*, 295501.
(47) Yang, J.; Chen, B.; Wang, H.; Mao, Q.; Imai, M.; Yoshimura, K.; Fang, M. Magnetic properties in layered ACo_2Se_2 (A = K, Rb, Cs) with the $ThCr_2Si_2$-type structure. *Phys. Rev. B: Condens. Matter Mater. Phys.* **2013**, *88*, 064406.
(48) Huang, J.; Wang, Z.; Pang, H.; Wu, H.; Cao, H.; Mo, S.-K.; Rustagi, A.; Kemper, A. F.; Wang, M.; Yi, M.; Birgeneau, R. J. Flatband-Induced Itinerant Ferromagnetism in $RbCo_2Se_2$. *Phys. Rev. B: Condens. Matter Mater. Phys.* **2021**, *103*, 165105.
(49) Schoop, L. M.; Pielnhofer, F.; Lotsch, B. V. Chemical Principles of Topological Semimetals. *Chem. Mater.* **2018**, *30*, 3155.

https://doi.org/10.1021/jacs.1c05107
J. Am. Chem. Soc. 2021, 143, 13646−13654